

Tracing the layers of Photodissociated gas in Trifid Nebula

BHASWATI MOOKERJEA¹ AND GÖRAN SANDELL²

¹*Department of Astronomy & Astrophysics, Tata Institute of Fundamental Research,
Homi Bhabha Road, Mumbai 400005, India*

²*Institute for Astronomy, University of Hawai'i at Manoa, Hilo,
640 N. Aohoku Place, Hilo, HI 96720, USA*

Submitted to APJ

ABSTRACT

Photodissociated gas bears the signature of the dynamical evolution of the ambient interstellar medium impacted by the mechanical and radiative feedback from an expanding H II region. Here we present an analysis of the kinematics of the young Trifid nebula, based on velocity-resolved observations of the far-infrared fine-structure lines of [C II] at 158 μm and [O I] at 63 μm . The distribution of the photodissociated regions (PDRs) surrounding the nebula is consistent with a shell-like structure created by the H II region expanding with a velocity of 5 km s⁻¹. Comparison of ratios of [C II] and [O I]63 μm intensities for identical velocity components with PDR models indicate a density of 10⁴ cm⁻³. The red- and blue-shifted PDR shells with a combined mass of 516 M_⊙ have a kinetic energy of $\sim 10^{47}$ erg. This is consistent with the thermal energy of the H II region as well as with the energy deposited by the stellar wind luminosity from HD 169442A, an O7 V star, over the 0.5 Myr lifetime of the star. The observed momentum of the PDR shell is lower than what theoretical calculations predict for the radial momentum due to the shell being swept up by an expanding H II region, which suggests that significant mass loss has occurred in M20 due to the dispersal of the surrounding gas by the advancing ionization front.

Keywords: ISM: clouds – ISM: kinematics and dynamics – submillimetre: ISM – ISM: structure – stars: formation – ISM:individual (M20)

1. INTRODUCTION

The Trifid nebula (M20) is an H II region with an age of approximately 0.5 Myr (Lefloch & Cernicharo 2000) ionized by the O7 V star HD164492A (Lynds et al. 1985) located in the Sagittarius spiral arm at a distance of 1180±25pc (Kuhn et al. 2021). Figure 1 shows a composite three-color optical image of M20 observed by Wolfgang Promper from his remote observatory in Namibia with narrowband filters, O III (*blue*), H α (*green*) and S II (*red*). The image shows both the large-scale filamentary dust feature and the denser gas towards the south-west that lie in front of the ionized gas in the H II region created by HD 164492A.

The Infrared Space Observatory (ISO) and Hubble Space Telescope (HST) observations (Cernicharo et al. 1998; Lefloch & Cernicharo 2000) show the Trifid to be a dynamic star-forming region containing young stellar objects (YSOs), many of them undergoing episodes of violent mass ejection or transferring mass and energy to the nebula in the form of jets. Comparison of a high-resolution radio continuum image at 20 cm and a CO map suggest that in its expansion the H II region has encountered a large dense molecular cloud to the south-west (SW), possibly triggering the formation of new stars (Cernicharo et al. 1998). From the Spitzer Infrared Array Camera (Spitzer/IRAC) and Multi-Band Imaging Photometer for Spitzer (MIPS) images of the Trifid nebula (M20), Rho et al. (2006) identified about 160 YSOs at different evolutionary stages distributed around the whole nebula, and beyond. These cover all stages of proto-stellar evolution, from Class 0 protostars to more evolved young stellar objects (YSOs). The youngest (Class 0/I protostars TC0–TC8) of the sources in the region are located within the dense far-IR and

millimetre cores identified in the 1.3 mm continuum map observed by Lefloch et al. (2002). In some of the dense cores evidence of jets originating from protostars have been discovered through narrow-band line imaging in the optical with the HST. Sticking out of the boundaries of one of the cores, TC2 is a 22-arcsec-long irradiated jet HH 399, ending close to a bow shock $\sim 1.5'$ away, in a low density environment (Cernicharo et al. 1998; Rosado et al. 1999; Yusef-Zadeh et al. 2005). Millimeter-wavelength molecular-line observations toward the nebula reveal several cloud components at velocities of $v_{\text{LSR}} \sim 2 \text{ km s}^{-1}$ (corresponding to the dark lanes crossing the optical nebula), $v_{\text{LSR}} \sim 8 \text{ km s}^{-1}$ (corresponding to dark features at the edge of the optical nebula), and $v_{\text{LSR}} \sim 18 \text{ km s}^{-1}$ (Kuhn et al. 2022; Cernicharo et al. 1998; Torii et al. 2011, 2017). A bridging feature between the 2 and 8 km s^{-1} clouds is seen coincident with the optical nebula and indicates that these clouds are physically interacting and may have collided (Haworth et al. 2015; Torii et al. 2017; Kalari 2021). Alternatively, the cloud kinematics could be interpreted as either an expanding H II region or turbulence (Fukuda & Hanawa 2000; Rho et al. 2008). Kuhn et al. (2022) used the $^{13}\text{CO}(2-1)$ channel maps to suggest that the 18 km s^{-1} cloud which is of much larger spatial extent is likely to be in the background. Until now studies of photodissociated gas in M20 have only been for a small region around the TC2 globule using the far- and mid-infrared fine-structure lines detected with the LWS and SWS onboard ISO (Lefloch et al. 2002).

Here we present a study of the photodissociated gas in an approximately $400' \times 400'$ region using the far-infrared (FIR) lines of [C II] at $158 \mu\text{m}$ and [O I] at $63 \mu\text{m}$ that account for most of the cooling. The datasets used here not only cover a much larger area compared to that studied by Lefloch et al. (2002) but also have the advantage of having higher spatial and more importantly spectral resolution compared to the ISO data. Recent velocity-resolved studies of Galactic PDRs have shown that both the [C II] and [O I] $63 \mu\text{m}$ emission are often moderately optically thick and sometimes significantly self-absorbed (Graf et al. 2012; Mookerjea et al. 2018; Guevara et al. 2020; Mookerjea et al. 2021). We use the velocity-resolved [O I] $63 \mu\text{m}$ and [C II] spectra to characterize the properties and distribution of the PDR gas vis-a-vis location of these components with respect to the ionizing source by segregating the major velocity components of both the diffuse and the dense PDR gas.

2. OBSERVATIONAL DATASETS

For this work, we have used several sets of publicly available data, which are described below.

2.1. GREAT/SOFIA observations

We have retrieved observations of the $^2\text{P}_{3/2} \rightarrow ^2\text{P}_{1/2}$ fine structure transition of ionized carbon (C^+) at 1900.5369 GHz ($157.74 \mu\text{m}$) and the $^3\text{P}_1 \rightarrow ^3\text{P}_0$ transition of atomic oxygen, [O I] $63 \mu\text{m}$, at 4,744.77749 THz of a region centered at the location of the TC2 globule ($(\alpha_{J2000}: 18^{\text{h}} 02^{\text{m}} 27.22^{\text{s}}, \delta_{J2000}: -23^{\circ} 04' 27''.5)$) in M20 from the data archive of the Stratospheric Observatory for Infrared Astronomy (SOFIA; Young et al. 2012). The observations (Id: 06.0041; PI: M. Kaufman) were carried out using the German REceiver for Astronomy at Terahertz frequencies (GREAT; Heyminck et al. 2012) on 2018 June 08. The GREAT was in the Low Frequency Array/High Frequency Array (LFA/HFA) configuration with both arrays operating in parallel. The LFA was tuned to [C II] and the HFA was tuned to [O I] $63 \mu\text{m}$. The beam sizes for the [C II] and [O I] $63 \mu\text{m}$ were $14''.1$ and $6''.3$ respectively. The [C II] map extends over a region of $400'' \times 400''$, while the usable part of the [O I] $63 \mu\text{m}$ is closer to $300'' \times 300''$. We used the Level 3b data available on the SOFIA archive for the region. All data were resampled to a spectral resolution of 0.5 km s^{-1} resulting in a median rms of 0.5 K for both [C II] and [O I] $63 \mu\text{m}$ data. The [O I] $63 \mu\text{m}$ map was smoothed with a Gaussian kernel and regridded to the same spatial resolution as the [C II] map, i.e. $14''.1$ (Fig. 2).

2.2. $^{12}\text{CO}(3-2)$ and $\text{HCO}^+(4-3)$ & $(1-0)$

For comparison with our observations, we used maps of the $J=3-2$ transition of ^{12}CO at 345795.9899 MHz at and the $J=4-3$ transition of HCO^+ at 356734.2230 MHz, both observed with the James Clerk Maxwell Telescope (JCMT) using the Heterodyne Array Receiver Program (HARP) receiver with a beam size of $14''$. The observations were performed as part of the proposal M07AH24A. The spectra were downloaded directly from the JCMT archive at the Canadian Astronomical Data Centre (CADC). The JCMT maps have a median rms of 0.3 K at a velocity resolution of 0.5 km s^{-1} . Additionally, $\text{HCO}^+(1-0)$ spectra observed with the IRAM 30m telescope as part of the Large Programme (LP017) for Master2 internships from Grenoble University, available at <https://www.iram.fr/ILPA/LP017/> were also used for comparison with the $\text{HCO}^+(4-3)$ data.

2.3. SEDIGISM

We have used the data cubes for $J=2-1$ transition of ^{13}CO and C^{18}O at 220398.68 and 219560.36 MHz respectively, that were observed as a part of the large-scale (84 deg^2) spectroscopic survey of the inner Galactic disk, named Structure, Excitation and Dynamics of the Inner Galactic Interstellar Medium (SEDIGISM; Schuller et al. 2021). These data were observed with the APEX telescope between 2013 and 2016 with an angular resolution of $30''$ and a 1σ sensitivity less than 1.0 K at 0.25 km s^{-1} velocity resolution. The SEDIGISM data were also used by Kuhn et al. (2022).



Figure 1. Composite three-color optical image of M20 observed by Wolfgang Promper from his remote observatory in Namibia with narrowband filters, OIII (*blue*), H α (*green*) and SII (*red*). The authors have obtained the permission to use the image available at <https://www.astronbin.com/2c61wh/B/?q=%22HD164294%22>

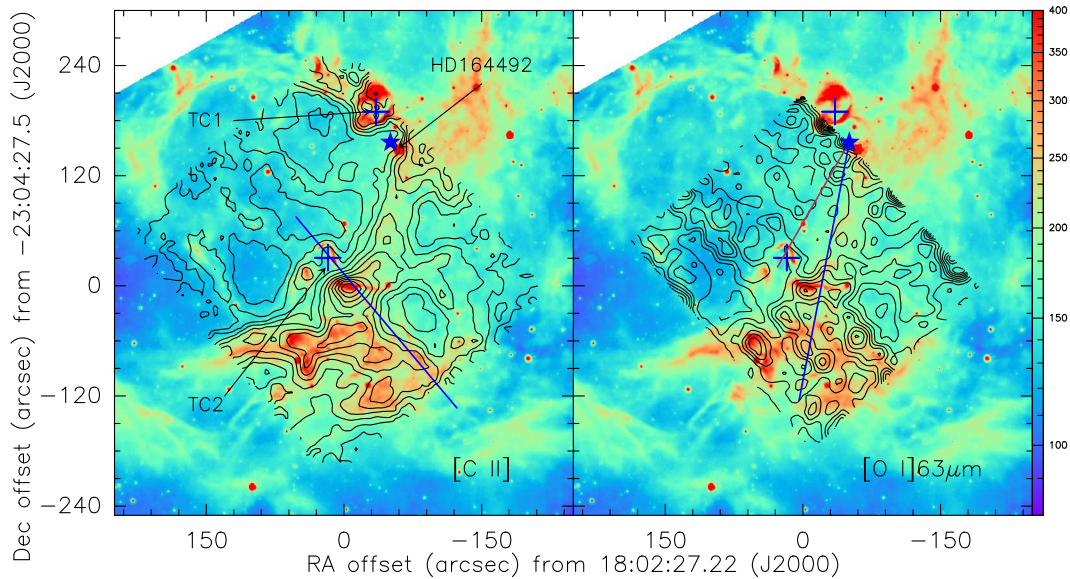


Figure 2. Contours of [C II] and [O I]63 μm intensities overlaid on color images of 8 μm Spitzer/IRAC region. Both maps are integrated between -4 to 14 km s^{-1} . The [C II] contours (in K km s^{-1}) correspond to 60 to 280 (in steps of 20) and the contours for [O I]63 μm are at 0.5, 3 to 30 (in steps of 3), 35, 40, 45, 50. The [C II] map is at the original resolution of $14''$, and the [O I]63 μm map is smoothed to the same resolution. The colorscale (in MJy sr^{-1}) for the 8 μm map is shown to the extreme right. The three solid straight lines correspond to directions along which position-velocity diagrams are analyzed (Fig. 7). Other important sources in the region are marked on both panels and labeled on the left panel.

3. MOLECULAR GAS DISTRIBUTION IN THE REGION

Figures 3 and A1 respectively, show the velocity-channel maps for the $^{13}\text{CO}(2-1)$ and $^{12}\text{CO}(3-2)$ emission in this region. The $^{13}\text{CO}(2-1)$ channel maps show emission mainly from the rims of the nebula, from the pillar containing TC2 and at velocities $>14 \text{ km s}^{-1}$. The $^{12}\text{CO}(3-2)$ channel map shows similar emission features except for the component beyond 14 km s^{-1} . The $^{13}\text{CO}(2-1)$ SEDIGISM channel maps were also analyzed by Kuhn et al. (2022), who write that the ^{13}CO emission is seen at

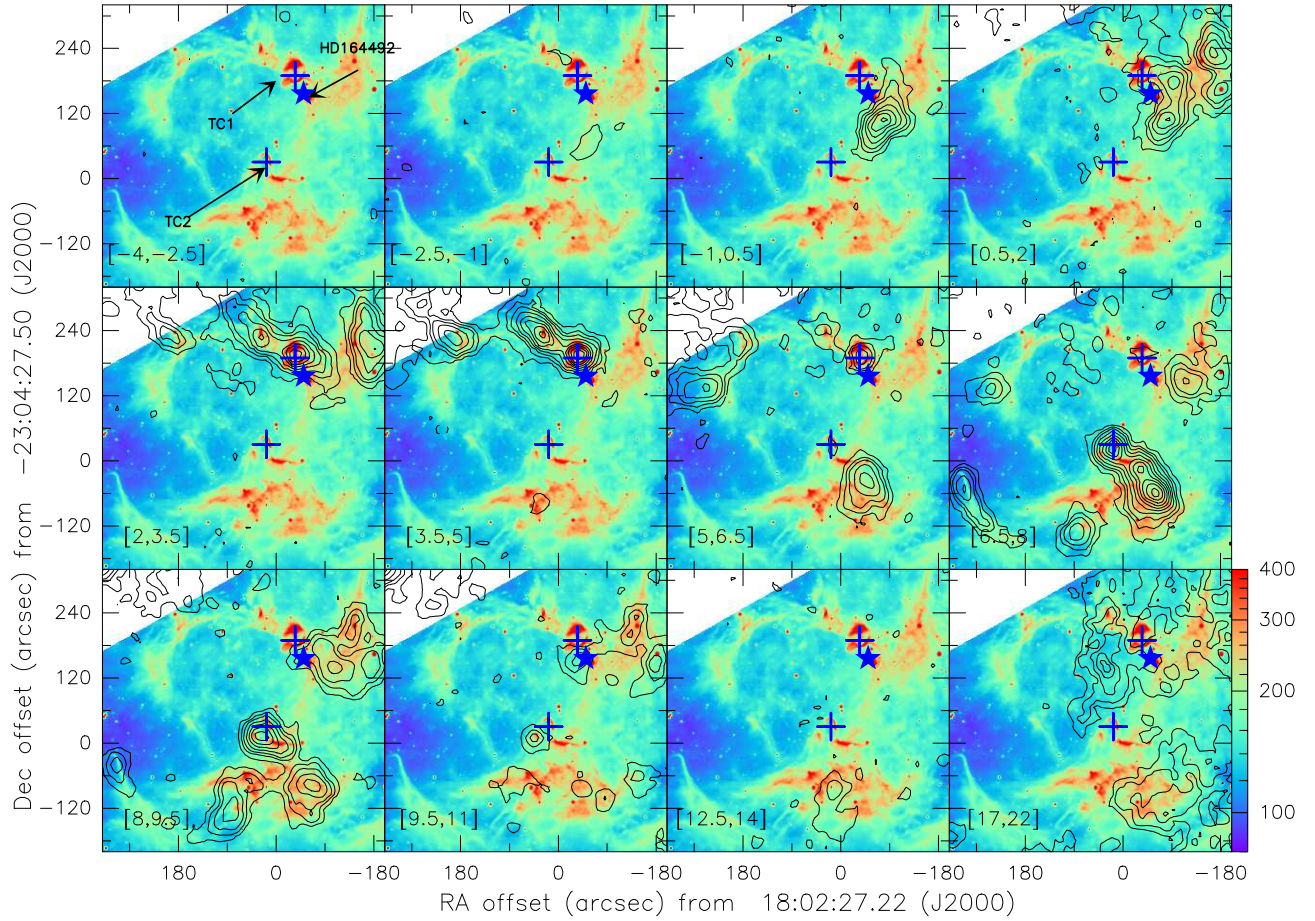


Figure 3. Map of $^{13}\text{CO}(2-1)$ emission in 1.5 km s^{-1} wide channels shown as contours overlaid on the Spitzer/IRAC $8 \mu\text{m}$ color image. The numbers in square brackets in each panel indicate the velocity range over which the emission was integrated. The bottom rightmost panel is an exception that shows intensity integrated over a wider velocity range of 17 to 22 km s^{-1} . The contours (in K km s^{-1}) are drawn at 1.5, 3, 4.5, 6, 7 to 28 in steps of 3. For the bottom right panel the levels (in K km s^{-1}) are at 6 to 18 in steps of 1. The color bar to the right shows the $8 \mu\text{m}$ intensity scale in units of MJy sr^{-1} . HD164492 is marked with a star symbol and the sources TC1 and TC2 are marked with '+' signs.

almost any velocity between -4 to 28 km s^{-1} but the emission does not necessarily originate from gas at the same distance. In the Galactic spiral arm model from Reid et al (2016), gas near the Sagittarius Arm is expected to have $v_{\text{LSR}} \approx 8 \text{ km s}^{-1}$ and gas in the near Scutum Arm would have $v_{\text{LSR}} \approx 18 \text{ km s}^{-1}$. Kuhn et al. (2022) argued that given the 18 km s^{-1} matches the expected velocity of the near Scutum Arm it is likely that the CO emission in the velocity range $v_{\text{LSR}} \approx 13-28 \text{ km s}^{-1}$ comes from a molecular cloud far behind Trifid. These authors concluded that the multiple peaks seen in the average spectrum of the region lying between 0 to 13 km s^{-1} are compatible with the acceleration of dense cloudlets during the shredding of the molecular cloud by the expanding H II region created by the radiative feedback due to HD 164492. They further noted that the observed velocities and structure are comparable to those obtained from numerical simulations of cloud disruption by radiative feedback (Ali et al. 2018; Fukushima et al. 2020).

4. VELOCITY DISTRIBUTION OF DIFFUSE AND DENSE PDR GAS

The fine structure lines [C II] at $158 \mu\text{m}$ and [O I] at $63 \mu\text{m}$ are widely regarded as the bona-fide tracers of the PDR gas. Owing to the significantly different excitation conditions, the two spectral lines are also useful to discriminate between the diffuse and dense PDR gas. The [C II] at $158 \mu\text{m}$ with an upper energy level of 91 K and a critical density of 3000 cm^{-3} is easily excited under average Galactic ISM conditions in which C^+ are found. The [O I] $63 \mu\text{m}$ line has an upper energy level of 227.7 K and a critical density of $2 \times 10^5 \text{ cm}^{-3}$. Thus, although atomic oxygen is as abundant as carbon the [O I] $63 \mu\text{m}$ emission arises primarily from high density PDRs. Utilising the velocity-resolved spectra for both tracers we attempt to localize the diffuse and dense PDR gas in a velocity-coherent manner.

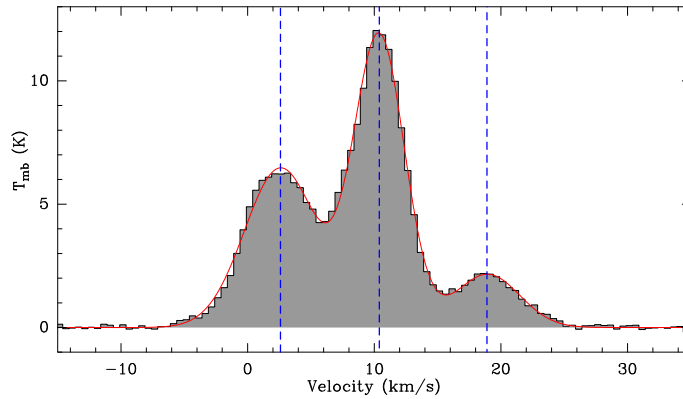


Figure 4. The [C II] spectrum averaged over the entire mapped region. The red curve shows a fit to the spectrum using a three-component Gaussian profile centered at 2.6, 10.4 and 18.9 km s⁻¹. The centers of the Gaussian components are marked by the vertical dashed lines.

Figure 2 suggests an overall similarity between the distribution of the velocity-integrated emission of [C II] and [O I]63 μm when both are integrated between -4 to 14 km s⁻¹. Both intensity maps trace the southern part of the region hosting the pillar and the TC2 globule and part of the dust lanes seen in the optical image across M20. In order to investigate the kinematics and distribution of the gas contributing to the emission of [C II] we examine the [C II] spectrum averaged over the entire mapped region (Fig. 4). Using a multi-component Gaussian fit to the average [C II] spectrum we identify three distinct velocity components approximately centered at 2.6, 10.4 and 18.9 km s⁻¹ – these components match well with the velocity components already identified in the molecular line data (Fig. 4).

The distribution of the PDR gas is traced more clearly in the channel maps of [C II] and [O I]63 μm (Fig. 5, 6). All the three velocity components are seen in the [C II] map. The [O I]63 μm map primarily traces the emission of the 8 km s⁻¹ component, but also shows some of the 2 km s⁻¹ velocity component, in particular the PDR emission from the dark dust lane bisecting the image. This PDR emission stands out in both [C II] and [O I]63 μm in the channels from -2.5 to +0.5 km s⁻¹, in contrast to the ¹³CO(2-1) and ¹²CO(3-2) emission which show very little emission at velocities < -1 km s⁻¹. The velocity component at +18 km s⁻¹ is strongly contaminated by telluric [O I] emission, which masks any [O I] emission in that velocity range. The northern ridge containing TC1 was only partially observed in the [O I]63 μm (Fig. 6). The 8 km s⁻¹ component is clearly visible in [C II], [O I]63 μm , ¹³CO(2-1) and ¹²CO(3-2) channel maps. Both [C II] and [O I]63 μm emission trace the pillar-like structure, with the TC2 globule at its head, at velocities between 5 to 9.5 km s⁻¹, whereas the emission from the velocities between 8 to 13 km s⁻¹ appear to be also tracing the denser gas located to the south-west of the map. The velocity-resolved observations suggest that the [C II] and [O I]63 μm emission as a function of velocity resemble emission from different photo-irradiated layers of the molecular cloud impacted by the expanding H II region. Such a scenario is further substantiated by the position-velocity (p - v hereafter) diagrams for both [C II] and [O I]63 μm (Fig. 7) along the three directions shown in the integrated intensity maps (Fig. 2). The clear circular shell generated in the [C II] p - v diagram by the 2 km s⁻¹ and 8 km s⁻¹ clouds is characteristic of the position-velocity diagram due to shell created by an expanding H II region. Additionally we notice that for the direction along the pillar with TC2, while the [O I]63 μm emission is centered at 8 km s⁻¹, the [C II] emission shows two branches with the branch around 10 km s⁻¹ being brighter. The ¹²CO(3-2) emission traces warmer and denser gas than the ¹³CO(2-1) emission and though the features seen in the position-velocity diagrams are closer to the structures seen in the [O I]63 μm , the blue-shifted half of the shell clearly detected in [C II] is also partially detected in ¹²CO(3-2) (Fig. A2).

In order to explore whether the split in emission in the 8 km s⁻¹ cloud seen in [C II] close to the bright emission regions arises due to opacity effects, we compared the [C II] and [O I]63 μm spectra with ¹³CO(2-1) SEDIGISM spectra and HCO⁺(1-0) spectra at twelve selected positions (Fig. 8). We find that at most positions where the [C II] spectra are double-peaked in the 8 km s⁻¹ component, the [O I]63 μm , ¹³CO(2-1) and HCO⁺ tend to align with one of the peaks and do not appear at the velocity where the [C II] spectra show the dip. Although restricted by the noise level, the C¹⁸O(2-1) spectra at those positions also show the peak to be aligned with one of the peaks, thus indicating that the two peaks correspond to emission from clouds at two velocities. The overlapping but distinctly different structures which manifest in the velocity ranges 6.5 to 8 km s⁻¹ and 9.5 to 11 km s⁻¹ in the [C II] channel map strongly suggest that the two peaks in the [C II] spectrum arise from different layers of the PDR separated in velocity. Fitting the 8 km s⁻¹ feature in the [C II] spectra in this region using Gaussian components we obtain velocities around 8.2 and 11 km s⁻¹ for the two components. The [O I]63 μm spectra at these positions also show two components centered around 7.8 and 10.8 km s⁻¹ while the ¹³CO(2-1) profiles can be fitted with a single component lying

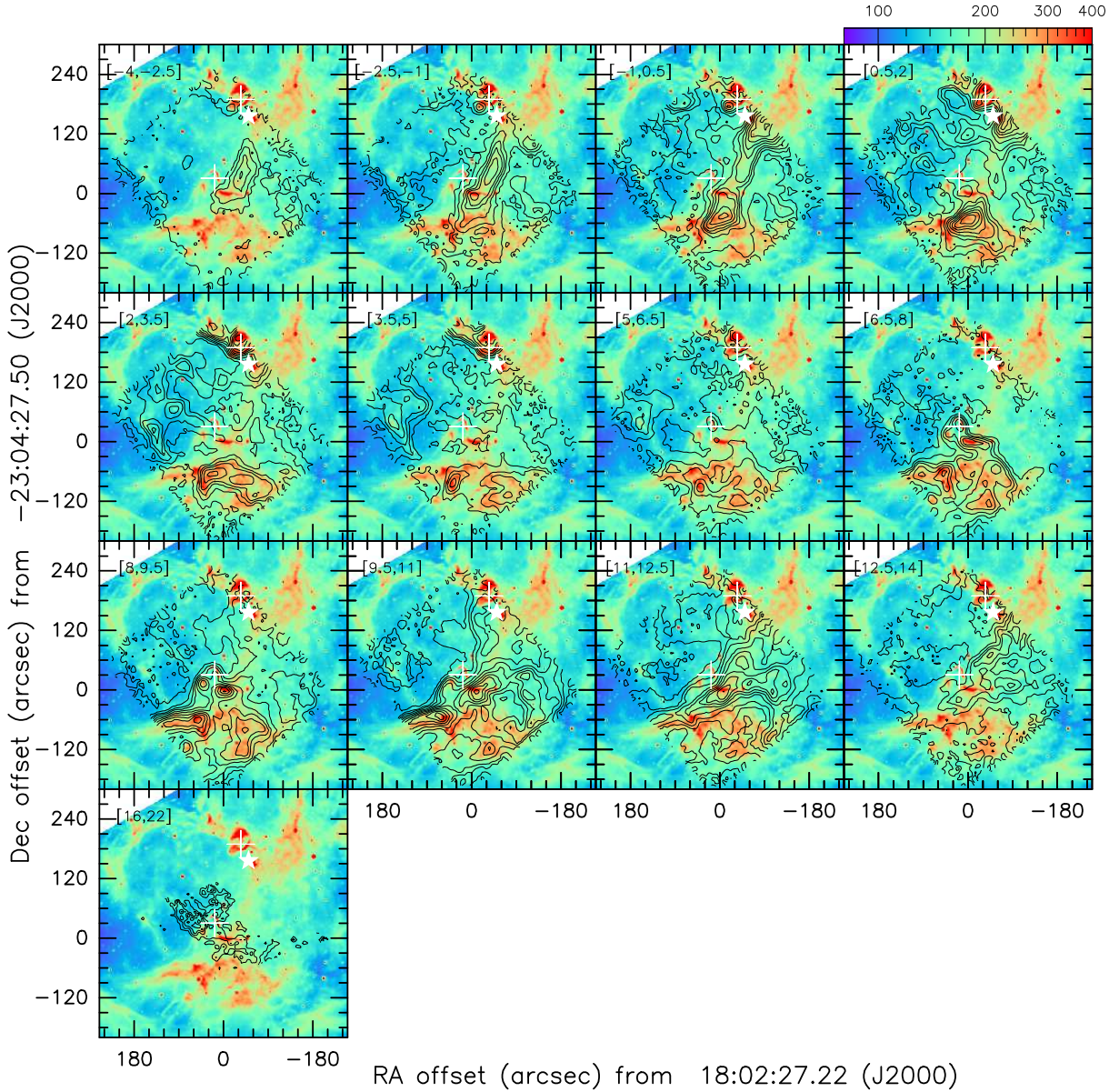


Figure 5. Map of [C II] emission in 1.5 km s^{-1} wide channels shown as contours overlaid on the Spitzer/IRAC $8 \mu\text{m}$ color image. The numbers in square brackets in each panel indicate the velocity range over which the emission was integrated. The contours are drawn at 0.5, 2.5, 4.5, 6 to 48 (K km s^{-1}) in steps of 6 K km s^{-1} . The lowermost panel is an exception that shows intensity integrated over a wider velocity range of 16 to 22 km s^{-1} with contours drawn at 15 to 23 K km s^{-1} in steps of 2 K km s^{-1} . The color bar on the top shows the $8 \mu\text{m}$ intensity scale in units of MJy sr^{-1} . HD164492 is marked with a star symbol and the sources TC1 and TC2 are marked with '+' signs. .

between 7 and 8.2 km s^{-1} as the RA offset ($\Delta\alpha$) changes from -42 to $28''$. Of the two velocity components, the $\sim 7 \text{ km s}^{-1}$ component appears to be due to denser gas, since it is detected in both [O I] $63 \mu\text{m}$ and $\text{HCO}^+(1-0)$. The $\sim 11 \text{ km s}^{-1}$ component in contrast is dominantly seen in the [C II] emission and hence is likely to be from more diffuse PDR gas.

4.1. Gaussian Decomposition of Spectra

We attempt to identify velocity-coherent features associated with the primary velocity features in the [C II], [O I] $63 \mu\text{m}$ and CO datasets. For this purpose we chose to use [C II] because of its sensitivity to both diffuse and dense PDR gas, hence tracing the overall kinematics better than the [O I] $63 \mu\text{m}$ emission. We have used the FUNStools.Decompose¹ to decompose the [C II] data

¹ <https://github.com/radioshiny/funstools>

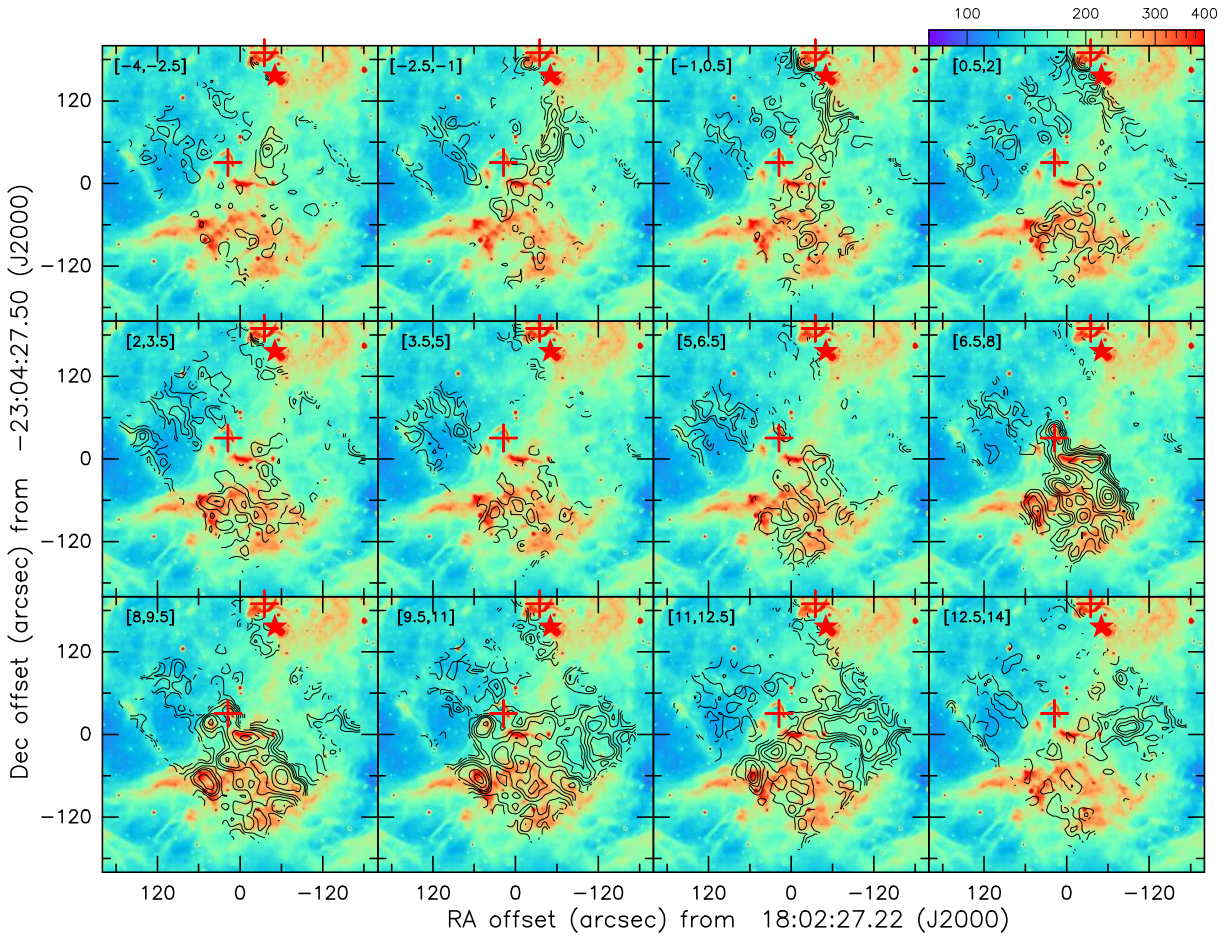


Figure 6. Map of [O I] $63 \mu\text{m}$ emission in 1.5 km s^{-1} wide channels shown both a color map and contours. The numbers in square brackets in each panel indicate the velocity range over which the emission was integrated. The contours (in K km s^{-1}) are drawn at 0.5, 1.0, 1.75, 2.5, 3.25, 5 to 20 in steps of 1. HD164492 is marked with an asterisk and the sources TC1 and TC2 are shown as '+'. The color bar on the top shows the $8 \mu\text{m}$ intensity scale in units of MJy sr^{-1} . HD164492 is marked with a star symbol and the sources TC1 and TC2 are marked with '+' signs.

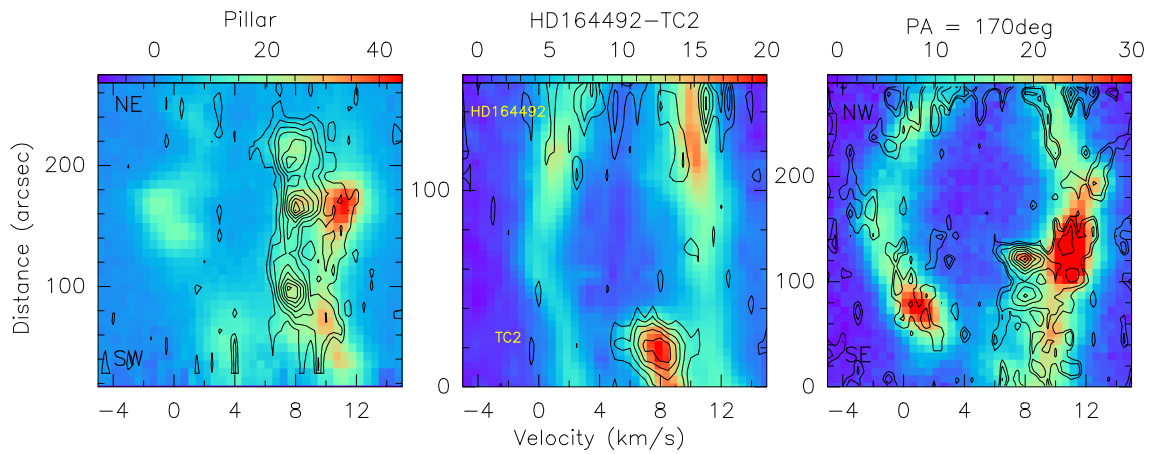


Figure 7. Position-velocity diagrams of [C II] emission along the cuts shown in Fig. 2. The contours are for the p - v diagram for [O I] $63 \mu\text{m}$ and correspond to the levels (Left) 1 to 14 K in steps of 1 K, (Middle) 1 to 30 K in steps of 1 K, and (Right) 0.5, 1 to 35 K in steps of 1 K. The colorbar on the top of each panel shows the [C II] intensities in K.

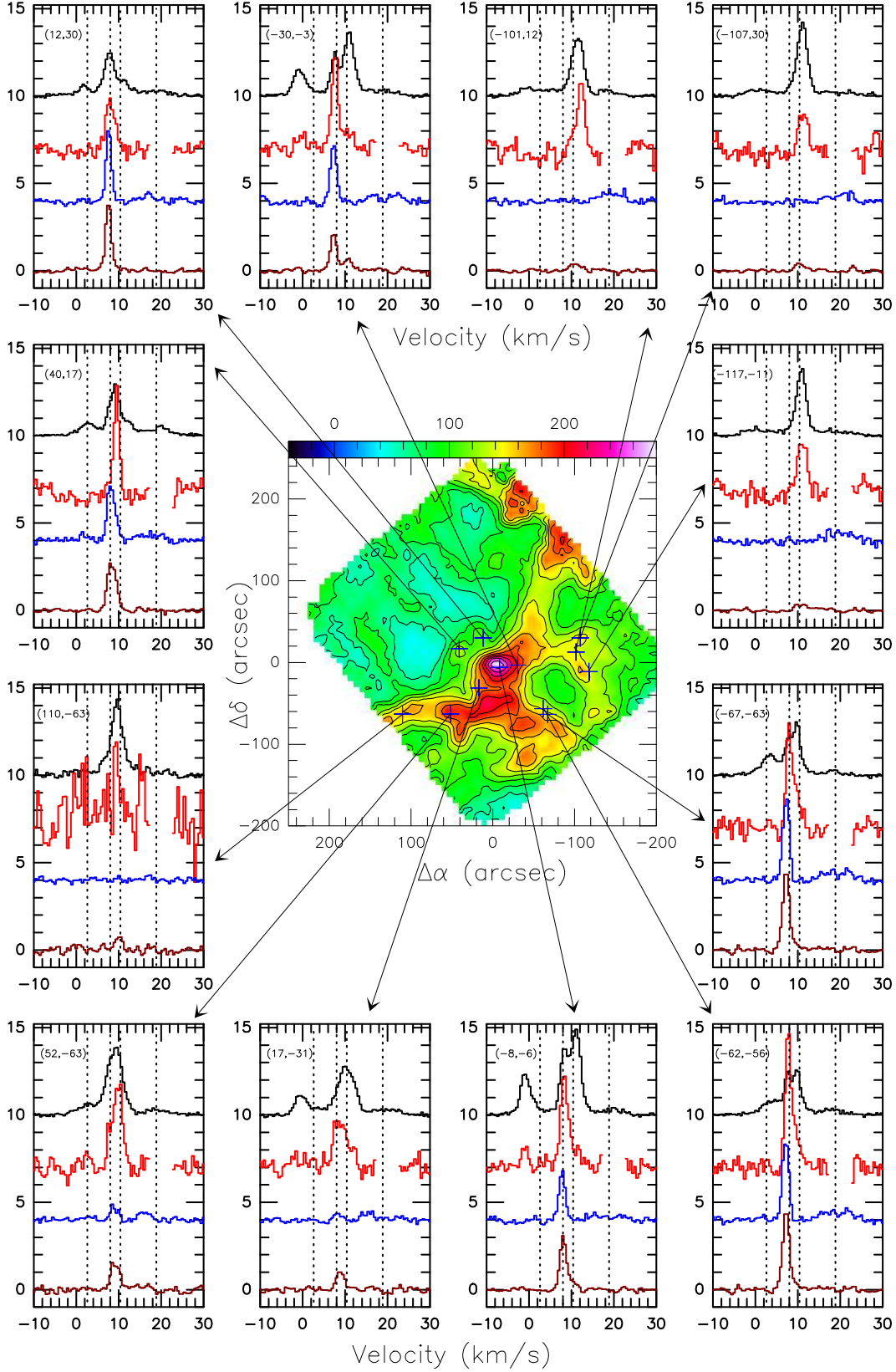


Figure 8. Comparison of [C II] (black), [O I]63 μm (red), $^{13}\text{CO}(2-1)$ (blue) and $\text{HCO}^+(1-0)$ (maroon) spectra at selected positions. The positions are shown on the [C II] intensity map integrated over -3 to 14 km s^{-1} . The contour levels in intensity map correspond to 60 to 280 K km s^{-1} in steps of 20 km s^{-1} and the offsets in are with respect to the same center as in Fig. 5. The y-axis for each spectrum corresponds to T_{mb} . The [C II], $^{13}\text{CO}(2-1)$ and $\text{HCO}^+(1-0)$ spectra are scaled by factors of 0.11 , 0.3 and 1.5 respectively. The [C II], [O I]63 μm and $^{13}\text{CO}(2-1)$ spectra are shifted along the y-axis for better visibility. Vertical dashed lines correspond to 2 , 8 and 18 km s^{-1} , respectively.

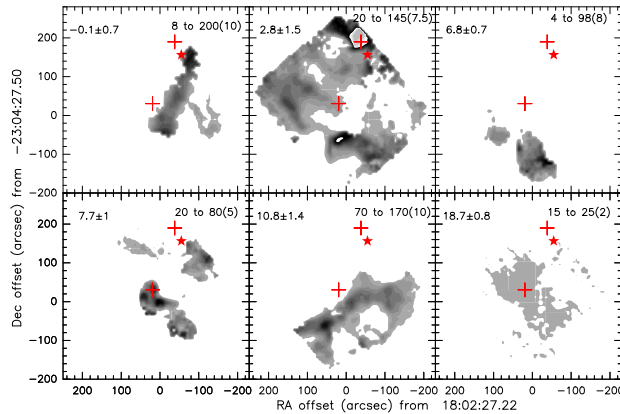


Figure 9. Velocity coherent structures identified in the region based on the [C II] spectra using Gaussian decomposition followed by the identification of groups using a friend-of-friend algorithm are shown as contours. The color image corresponds to the velocity-integrated [C II] emission and the colorscale is shown at the top of the figure. In each panel we indicate the mean velocity of the group along with the standard deviation in km s^{-1} on the left and the contour levels in units of K km s^{-1} on the right.

cubes into multiple Gaussian components. The tool is based on an algorithm that primarily decides the number of components and their velocity positions in the smoothed spectrum using the first, second, and third derivatives based on the idea that a genuine velocity component is continuous with the surroundings. The results of the first fitting are given as the initial guess to a subsequent round of Gaussian fitting in an iterative manner. The outcome are the parameters such as the central velocity and the linewidth for each velocity component identified at each pixel in the [C II] datacube. Subsequently, we identify coherent structures corresponding to each of the velocity components so identified by applying the friends-of-friends (FoF) technique to the central velocity of each of the components. The algorithm works in an iterative manner in which it first selects the decomposed Gaussian seed component with the maximum amplitude and gives the structure a number. Subsequently the other Gaussian components in the neighboring pixels whose pixel distance is less than $\sqrt{2}$ from the seed component are selected, and the velocity differences of the seed and other components in the neighboring pixels are checked. If the the velocity difference between the seed and other components in the neighboring pixel is less than the velocity dispersion of the seed ($\sigma_{\nu}^{\text{seed}}$) the neighboring component is identified as a friend of the seed and assigned the same group number. If more than one velocity component in a neighboring pixel is within the range of velocity dispersion from the velocity of the seed, then only the closest one becomes the friend of the seed. In the next iteration the assigned friends of the seed become the seeds of the structure and the same procedure is repeated until there are no more friends to assign.

Using this method of identification of velocity-coherent structures in the [C II] emission, we identify 5 main velocity components with velocities (in km s^{-1}) centered at -0.1 ± 0.7 , 2.8 ± 1.5 , 6.8 ± 0.7 , 7.7 ± 0.1 , 10.8 ± 1.4 . Additionally we detect the component at $18.7 \pm 0.8 \text{ km s}^{-1}$, which as mentioned earlier is unrelated to M20 and most probably associated with the Scutum arm. While the outcome is consistent with the channel maps, decomposition of the spectra into Gaussian components helps us to isolate the overlapping features. This is particularly true for the features with mean velocities at 6.8, 7.7 and 10.8 km s^{-1} .

A combination of the features seen in the channel maps of [C II], and [O I]63 μm and grouping of the components identified in the Gaussian decomposition of [C II] spectra provides us with a three-dimensional view of the multiple layers of PDR shells associated with HD164492A.

5. DISCUSSION

5.1. Properties of the PDR shells

The velocity-resolved spectra of [C II] and [O I]63 μm have enabled us to identify the red- and blue-shifted parts of the far-ultraviolet (FUV; 6-13.6 eV) irradiated molecular shell created by the expanding H II region in M20. The structure seen particularly in the [C II] p - v plots (Fig. 7) along selected directions suggests that the emission between -5 to 5 km s^{-1} belongs to the blue-shifted (foreground) part of the shell, while the 5 to 15 km s^{-1} emission corresponds to the red-shifted part. The Gaussian decomposition of the spectra followed by identification of velocity-coherent emission features identifies two and three sub-structures in the blue- and red-shifted parts of the shell, respectively (Fig. 9). The detection of brighter [O I]63 μm emission from the red-shifted part of the shell indicates that it has higher density than the blue-shifted part. Previous studies of Galactic PDRs have shown that the [C II] emission is often optically thick, while the [O I]63 μm spectra are affected by foreground low-excitation gas with atomic oxygen. Since we did not detect [$^{13}\text{C II}$], which would have enabled us to determine the optical

depth of the [C II] emission, we instead use the results from [Lefloch et al. \(2002\)](#), who estimated that the kinetic temperature of the PDR gas was 300 K, to derive the column density $N(\text{C}^+)$. Since it is likely that the 5–15 km/s PDR emission has high density, for this part of the shell we adopt an optical depth of 2, a value typically seen in Galactic PDRs ([Mookerjea et al. 2018](#)). We assume the -5 to +5 km/s PDR emission to be optically thin. Equation (26) from [Goldsmith et al. \(2012\)](#) when modified for optically thick emission for the red-shifted shell, is as follows:

$$N(\text{C}^+) = 2.91 \times 10^{15} \left[1 + 0.5e^{91.25\text{K}/T_{\text{kin}}} \left(1 + \frac{A_{\text{ul}}}{C_{\text{ul}}} \right) \right] \frac{\tau}{1 - e^{-\tau}} \int T_{\text{mb}} dv \quad (1)$$

where $A_{\text{ul}} = 2.3 \times 10^{-6} \text{ s}^{-1}$, T_{kin} is the gas kinetic temperature, the collision rate is $C_{\text{ul}} = R_{\text{ul}}n$ with R_{ul} being the collision rate coefficient with H_2 or H^0 , which depends on T_{kin} , and n is the volume density of H. Since the critical density of the [C II] transition is $n_{\text{cr}}=3000 \text{ cm}^{-3}$, and since it is likely that most of the [C II] detected could be at such densities along with some emission arising from clumps with densities exceeding 10^5 cm^{-3} , we assume a density of 10^4 cm^{-3} to estimate the $N(\text{C}^+)$ density distribution of the PDR gas. For this calculation we consider excitation of [C II] due to C^+-H_2 collisions, with $R_{\text{ul}} = 3.8 \times 10^{-10} \text{ cm}^3 \text{ s}^{-1}$. The value of $N(\text{C}^+)$ estimated for the red-shifted shell is between $(1-3) \times 10^{18} \text{ cm}^{-2}$, while for the blue-shifted shell $N(\text{C}^+)$ ranges between $(2-9) \times 10^{17} \text{ cm}^{-2}$. Based on LWS observations with a beam size of $45''$ [Lefloch et al. \(2002\)](#) had estimated that $N(\text{C}^+)$ in the PDR of the globule is around $(4.5-5.7) \times 10^{17} \text{ cm}^{-2}$, after subtracting a 30% contribution to [C II] emission from the ionized gas in the H II region. At TC2, we estimate a total $N(\text{C}^+)$ of $1.2 \times 10^{18} \text{ cm}^{-2}$ and if 30% of the [C II] emission were to arise from the ionized gas, the contribution of the PDR will be $\sim 8.4 \times 10^{17} \text{ cm}^{-2}$. Within the limits of the uncertainties this estimate is consistent with the values determined by [Lefloch et al. \(2002\)](#).

In order to examine the properties of the PDRs created in the FUV irradiated parts of the red- and blue-shifted molecular shells we derive the [C II]/[O I]63 μm intensity ratios for both components. The area over which the ratio can be determined is restricted by the usable pixels of the [O I]63 μm map. For the red and the blue-shells the [C II]/[O I]63 μm intensity ratios (in energy units) vary between (0.8 to 2.5) and (1 to 1.5), respectively. [Lefloch et al. \(2002\)](#) estimated the FUV field intensity at the location of the globule TC2 due to HD 164492A to be $G_0 = 1000$. Comparison of the observed [C II]/[O I]63 μm intensity ratios with the results of the Kaufman PDR model ([Kaufman et al. 2006](#)) for an FUV intensity of $G_0=1000$ suggest densities of 4×10^3 and 500 cm^{-3} for the red and the blue-shifted shells. Based on the detection of [O I]63 μm emission, it appears that these densities are lower limits. The lower derived values of the density could be because the volume and hence beam-filling factor of the [C II] emission is likely to be significantly larger than the [O I]63 μm emission that arise from high density PDRs and this could lead to higher values of observed [C II]/[O I]63 μm intensity ratios, which imply lower densities. At the position corresponding to TC2 ($40''$, $17''$) we have fitted the [O I]63 μm spectrum using a single velocity component Gaussian profile resulting in $v_{\text{LSR}} = 9.5 \text{ km s}^{-1}$ and $\Delta v = 1.6 \text{ km s}^{-1}$. The [C II] spectrum at this position between -8 to 17 km s^{-1} shows three velocity components, hence we have fitted it with three Gaussians. While fitting the [C II] profile we kept the center and the width of one of the components fixed at the fitted values obtained for the [O I]63 μm profile. Thus, for this velocity component, which is seen in both the [C II] and [O I]63 μm emission, we estimate a [C II]/[O I]63 μm intensity ratio (in energy units) of 0.2. For such a ratio and a $G_0 = 1000$, the PDR models indicate a density of 10^4 cm^{-3} .

5.2. Kinematics of the PDR shells

Based on the [C II] intensities, we estimate the total integrated column densities ($N(\text{C}^+)$) of the blue- and the red-shifted shells to be 5.9×10^{20} and $2.4 \times 10^{21} \text{ cm}^{-2}$, respectively. Considering a C/H_2 ratio of 1.5×10^{-4} at the distance of M20 (1180 pc), the masses of the blue- and red-shifted shells are estimated to be 100 and $416 M_{\odot}$, respectively. Based on the shells identified in the position-velocity plots of [C II] (Fig. 7), we estimate the median expansion velocity of the shells to be $\sim 5 \text{ km s}^{-1}$. Thus the total kinetic energy of the PDR shells is approximately $1.3 \times 10^{47} \text{ erg}$. [Chaisson & Willson \(1975\)](#) derived a few parameters for the H II region M20, created by the star HD169942A: it extends over $5'3 \times 6'4$, which at a distance of 1180 pc corresponds to a size of $1.8 \times 2.2 \text{ pc}$, has an average electron density (n_e) of $100-150 \text{ cm}^{-3}$ and has an electron temperature (T_e) of 8150 K. [García-Rojas et al. \(2006\)](#) estimated the electron number density to be $270 \pm 60 \text{ cm}^{-3}$. The total thermal energy of the H II region written as $E_{\text{th}} = \frac{3}{2} n_e \frac{4\pi}{3} R^3 k_B T_e$, where R is the radius of the H II region and k_B is the Boltzmann constant. Based on these parameters we estimate the total thermal energy of the H II region to be $6 \times 10^{46} \text{ erg}$. Thus, subject to uncertainties of the electron density in the H II region, the kinetic energy of the PDR shell is about two times the thermal energy of the H II region.

The photoionized gas in the interior of an expanding H II region exerts a pressure force and delivers outward radial momentum and kinetic energy to the swept-up shell. For a spherical H II region the momentum delivered to the ambient medium is ([Krumholz 2017](#)):

$$p_{\text{sh}} = 1.5 \times 10^5 \left[\frac{n_{\text{H}}}{10^2} \right]^{-1/7} \left[\frac{T_e}{10^4} \right]^{-8/7} \left[\frac{N_{\text{Ly}\alpha}}{10^{49}} \right]^{4/7} \left[\frac{t}{10^6} \right]^{9/7} M_{\odot} \text{ km s}^{-1}. \quad (2)$$

where n_{H} is the number density of hydrogen in the ambient medium, T_e is the electron temperature, $N_{\text{Ly}\alpha}$ is the Lyman continuum photon rate due to HD164492A and t is the age of the H II region. Lefloch & Cernicharo (2000) estimated the density of the shell to be 10^5 cm^{-3} and mean density of the cloud to be $2 \times 10^3 \text{ cm}^{-3}$. We note that the assumption of the H II region expanding in a uniform density environment could lead to uncertainties in the determination of its age and subsequently in the value of the density as well. In order to include the effects of higher density material that the expanding H II region would necessarily encounter in an otherwise clumpy molecular cloud, we assume the ambient density to be 10^4 cm^{-3} . For HD 164492A, an O7V type star the Lyman continuum photon rate is $5.6 \times 10^{48} \text{ s}^{-1}$ (Martins et al. 2005). Using Eq. (2) for the estimated age of the M20 nebula of 0.5 Myr we estimate the total momentum of the PDR shell to be $2.8 \times 10^4 M_{\odot} \text{ km s}^{-1}$. From the observations we estimate the momentum of the PDR shell with a mass of $516 M_{\odot}$ moving with a velocity of 5 km s^{-1} to be $\sim 2.6 \times 10^3 M_{\odot} \text{ km s}^{-1}$, which is lower by a factor of 10 than the p_{sh} estimated from Eq.(2). This could be due to the molecular (and photodissociated) material which might have been dispersed, hence carrying away part of the momentum.

The kinetic energy of the swept up shell is given by (Krumholz 2017):

$$E_{\text{sh}} = 8.1 \times 10^{47} \left[\frac{n_{\text{H}}}{10^2} \right]^{-10/7} \left[\frac{T_e}{10^4} \right]^{10/7} \left[\frac{N_{\text{Ly}\alpha}}{10^{49}} \right]^{5/7} \left[\frac{t}{10^6} \right]^{6/7} \text{ erg} \quad (3)$$

The kinetic energy of the swept up shell estimated using Eq. (3) is $3.1 \times 10^{44} \text{ erg}$, which is much smaller than the observed value by a factor of more than 320. It is clear that a simplistic model of an H II region expanding thermally in a uniform density environment cannot provide the observed kinetic energy of the shell. on the other hand, the wind luminosity from HD169942A is estimated to be $1.7 \times 10^{36} \text{ erg s}^{-1}$ (Rho et al. 2008; Howarth & Prinja 1989; Prinja et al. 1990), indicating that the wind has pumped in a total kinetic energy of $5.2 \times 10^{46} \text{ erg}$ over the 0.5 Myr lifetime of the Trifid nebula. This number matches quite well with the observed kinetic energy of the PDR shells as well as with the thermal energy of the ionized gas in the nebula.

6. SUMMARY & CONCLUSIONS

We have analysed the distribution of the PDR surfaces created by the FUV radiation from the O-type star HD 164492 that illuminates the H II region associated with the M20 nebula based on decomposition of the [C II] emission into velocity components. We disentangle the high density PDR material using the [O I]63 μm emission. The structure of the PDRs is consistent with shells created by the H II region expanding approximately with a velocity of 5 km s^{-1} . Based on the [C II]/[O I]63 μm intensity ratios we estimate the densities of the red and the blue-shifted parts to be 4000 and 500 cm^{-3} , which are likely to be the lower limits considering the possible mismatch between the beam-filling factors of the [C II] and the [O I]63 μm emission. The ratio, when estimated by considering the intensities of velocity components seen in both the [C II] and [O I]63 μm emission, suggest a density of 10^4 cm^{-3} , which is consistent with the ambient PDR density determined by Lefloch et al. (2002). The total kinetic energy estimated for the shells, $\sim 10^{47} \text{ erg}$, is consistent with both the thermal energy of the H II region as well as the total kinetic energy pumped in by the stellar wind during the lifetime (0.5 Myr) of the nebula. This is also an indirect confirmation of the age of the nebula. The total momenta of the detected parts of the shell is about $2.6 \times 10^3 M_{\odot} \text{ km s}^{-1}$, which is about ten times less than the momentum that a spherical H II region with the physical parameters of M20 can deliver. The presence of ‘‘holes’’ on either side of the dark lanes, which essentially are remnants of the blue-shifted part of the shell, also suggest that a significant part of this shell (molecular and/or PDR) has been blown away by the H II region and by the stellar wind. The material thus lost would have carried with it significant momentum and hence explains the discrepancy between the measured momentum of the shell and the momentum that the H II region is likely to deliver.

Radiative and mechanical feedback due to the massive stars both at the end of their lives (in the form of supernovae) and in their youth (as expanding H II regions and stellar winds) influence the triggering and/or hindrance to the formation of new generation of stars. The relative importance of the H II regions and the stellar winds in shaping the structure of the ambient interstellar medium is of interest in the context of the evolution of the Galactic interstellar medium and star formation scenario (cf. Pabst et al. 2020; Tiwari et al. 2021, and references therein). This work presented observational evidence of the role of the stellar winds in shaping the structure of the putative sites of triggered star formation in the Trifid nebula. The velocity information in the [C II] data enabled us to quantitatively compare the stellar wind inputs with the kinetic energy of the PDR shells and confirm that in this case the stellar winds provide the energy for expansion rather than the thermal expansion of the H II region. For a more comprehensive understanding of the kinematics of the M20 nebula, extending [C II] map to the north and obtaining a larger [O I]63 μm map would enable a quantitative analysis of TC1 similar to the analysis done by Lefloch et al. (2002) for TC2. Such

studies are crucial to obtain an improved understanding of the role of stellar feedback in determining the structure of the ambient medium that possibly trigger the formation of a new generation of stars in the region.

1 BM acknowledges the support of the Department of Atomic Energy, Government of India, under Project Identification No. RTI
2 4002 and the software related discussions with Akhil Lasrado. This research has made use of the NASA/IPAC Infrared Sci-
3 ence Archive, which is funded by the National Aeronautics and Space Administration and operated by the California Institute
4 of Technology. This publication is based on data acquired with the Atacama Pathfinder Experiment (APEX) under programmes
5 092.F-9315 and 193.C-0584. APEX is a collaboration among the Max-Planck-Institut für Radioastronomie, the European South-
6 ern Observatory, and the Onsala Space Observatory. The processed data products are available from the SEDIGISM survey
7 database located at <https://sedigism.mpifr-bonn.mpg.de/index.html>, which was constructed by James Urquhart and hosted by the
8 Max Planck Institute for Radio Astronomy. This research used the facilities of the Canadian Astronomy Data Centre operated
9 by the National Research Council of Canada with the support of the Canadian Space Agency. This work is based [in part] on
10 observations made with the Spitzer Space Telescope, which is operated by the Jet Propulsion Laboratory, California Institute
11 of Technology under a contract with NASA. This dataset or service is made available by the Infrared Science Archive (IRSA)
12 at IPAC, which is operated by the California Institute of Technology under contract with the National Aeronautics and Space
13 Administration.

APPENDIX

Here we present additional CO(3-2) channel maps and position-velocity diagrams.

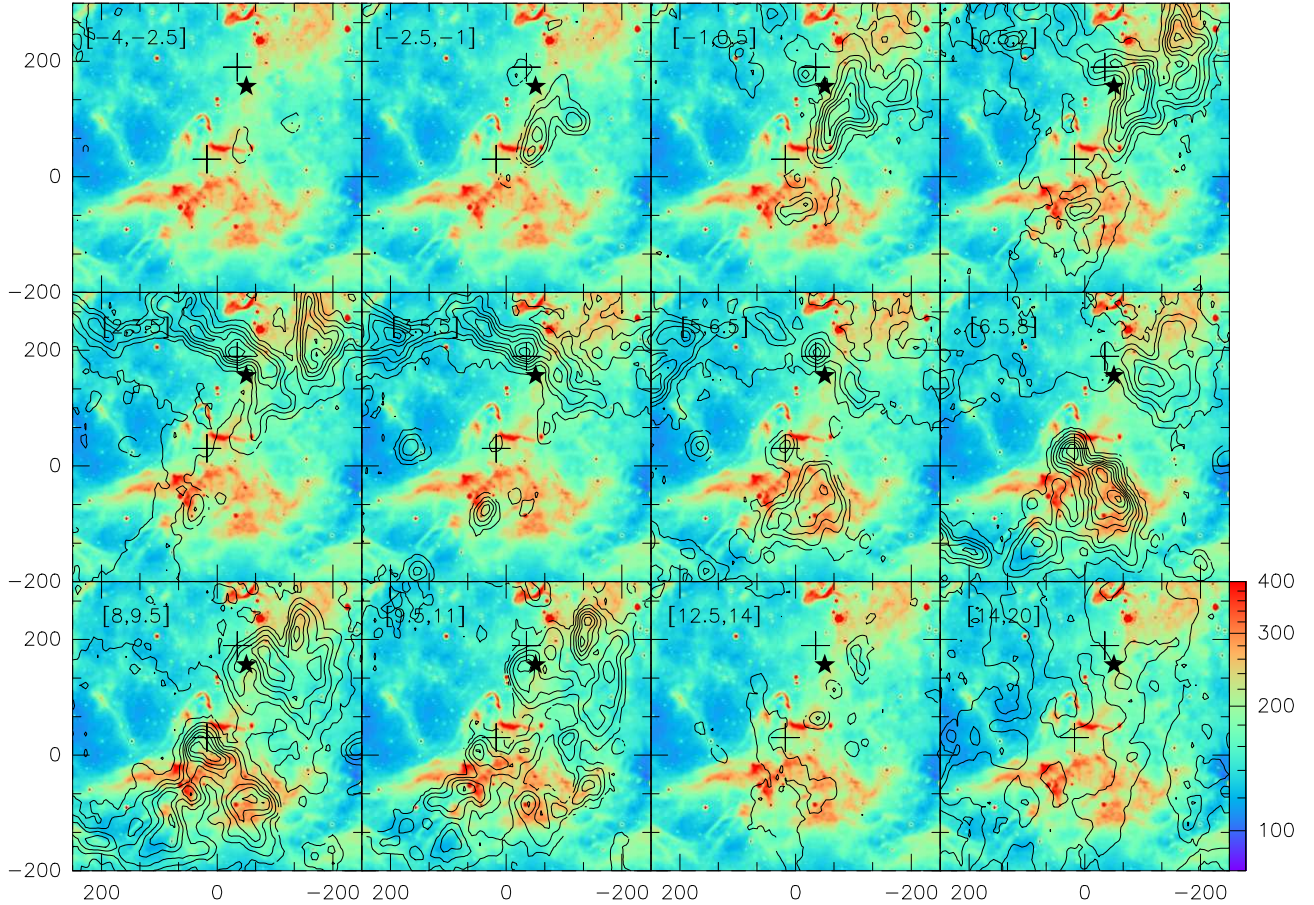
A. CHANNEL MAP AND POSITION-VELOCITY PLOTS FOR $^{12}\text{CO}(3-2)$ 

Figure A1. Map of $^{12}\text{CO}(3-2)$ emission in 1.5 km s^{-1} wide channels shown as contours overlaid on the Spitzer/IRAC $8 \mu\text{m}$ color image. The numbers in square brackets in each panel indicate the velocity range over which the emission was integrated. The bottom rightmost panel is an exception that shows intensity integrated over a wider velocity range of 14 to 20 km s^{-1} . The contours are drawn at 0.5, 2.5, 4.5, 6 to 48 (K km s^{-1}) in steps of 6 K km s^{-1} . The color bar to the right shows the $8 \mu\text{m}$ intensity scale in units of MJy sr^{-1} . HD164492 is marked with a star symbol and the sources TC1 and TC2 are marked with '+' signs.

Facility: IRSA, Spitzer, Herschel, SOFIA

REFERENCES

- Ali, A., Harries, T. J., & Douglas, T. A. 2018, *MNRAS*, 477, 5422
- Cernicharo, J., Lefloch, B., Cox, P., et al. 1998, *Science*, 282, 462
- Chaisson, E. J., & Willson, R. F. 1975, *ApJ*, 199, 647
- Fukuda, N., & Hanawa, T. 2000, *ApJ*, 533, 911
- Fukushima, K., Yamaguchi, H., Slane, P. O., et al. 2020, *ApJ*, 897, 62
- García-Rojas, J., Esteban, C., Peimbert, M., et al. 2006, *MNRAS*, 368, 253
- Goldsmith, P. F., Langer, W. D., Pineda, J. L., & Velusamy, T. 2012, *ApJS*, 203, 13
- Graf, U. U., Simon, R., Stutzki, J., et al. 2012, *A&A*, 542, L16
- Guevara, C., Stutzki, J., Ossenkopf-Okada, V., & et al. 2020, *A&A*, 636, A16

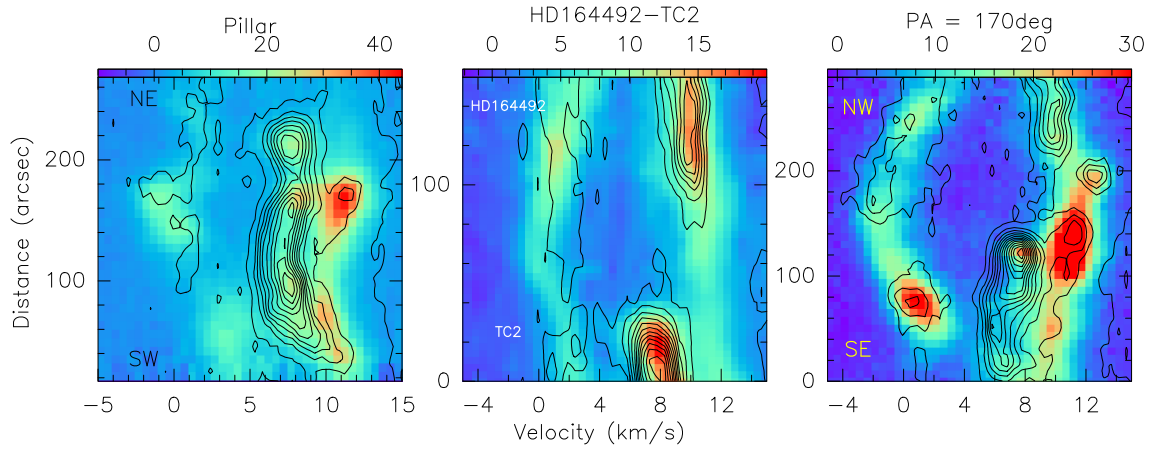


Figure A2. Position-velocity diagrams of $^{12}\text{CO}(3-2)$ emission along the cuts shown in Fig. 5 shown as contours overplotted on the color image of the [C II] p - v diagram. The contour levels are for T_{mb} from 1 to 32 K in steps of 3 K for the left panel and from 1 to 27 K in steps of 2 K for right panel. The colorbar on the top of each panel shows the [C II] intensities in K.

Haworth, T. J., Tasker, E. J., Fukui, Y., et al. 2015, MNRAS, 450, 10
 Heyminck, S., Graf, U. U., Güsten, R., et al. 2012, A&A, 542, L1
 Howarth, I. D., & Prinja, R. K. 1989, ApJS, 69, 527
 Kalari, V. M. 2021, ApJ, 921, 81
 Kaufman, M. J., Wolfire, M. G., & Hollenbach, D. J. 2006, ApJ, 644, 283
 Krumholz, M. R. 2017, Star Formation, doi:10.1142/10091
 Kuhn, M. A., Hillenbrand, L. A., Feigelson, E. D., et al. 2022, ApJ, 937, 46
 Kuhn, M. A., Benjamin, R. A., Zucker, C., et al. 2021, A&A, 651, L10
 Lefloch, B., & Cernicharo, J. 2000, ApJ, 545, 340
 Lefloch, B., Cernicharo, J., Rodríguez, L. F., et al. 2002, ApJ, 581, 335
 Lynds, B. T., Canzian, B. J., & Oneil, E. J., J. 1985, ApJ, 288, 164
 Martins, F., Schaerer, D., & Hillier, D. J. 2005, A&A, 436, 1049
 Mookerjee, B., Sandell, G., Vacca, W., & et al. 2018, A&A, 616, A31
 Mookerjee, B., Sandell, G., Veena, V. S., et al. 2021, A&A, 648, A40

Pabst, C. H. M., Goicoechea, J. R., Teyssier, D., et al. 2020, A&A, 639, A2
 Prinja, R. K., Barlow, M. J., & Howarth, I. D. 1990, ApJ, 361, 607
 Rho, J., Lefloch, B., Reach, W. T., & Cernicharo, J. 2008, in Handbook of Star Forming Regions, Volume II, ed. B. Reipurth, Vol. 5, 509
 Rho, J., Reach, W. T., Lefloch, B., & Fazio, G. G. 2006, ApJ, 643, 965
 Rosado, M., Esteban, C., Lefloch, B., Cernicharo, J., & García López, R. J. 1999, AJ, 118, 2962
 Schuller, F., Urquhart, J. S., Csengeri, T., et al. 2021, MNRAS, 500, 3064
 Tiwari, M., Karim, R., Pound, M. W., et al. 2021, ApJ, 914, 117
 Torii, K., Enokiya, R., Sano, H., et al. 2011, ApJ, 738, 46
 Torii, K., Hattori, Y., Hasegawa, K., et al. 2017, ApJ, 835, 142
 Young, E. T., Becklin, E. E., Marcum, P. M., et al. 2012, ApJL, 749, L17
 Yusef-Zadeh, F., Biretta, J., & Wardle, M. 2005, ApJ, 624, 246